Research Article | Vol. 28, No. 22 / 26 October 2020 / Optics Express 32750
Optics EXPRESS

Three dimensional drift control at nano-scale in single molecule localization microscopy

XIAOMING FAN,[1,2,3] THOMAS GENSCH,[2] GEORG BÜLDT,[3] YUANHENG ZHANG,[1,4] ZULIPALI MUSHA,[1,4] WENYUAN ZHANG,[1,4] RENZA RONCARATI,[1] AND RUIMIN HUANG[1,4,*]

[1]*Shanghai Institute of Materia Medica, Chinese Academy of Sciences, 201203 Shanghai, China*
[2]*Institute of Complex Systems (ICS-4, Cellular Biophysics), Forschungszentrum Jülich, Wilhelm-Jonen-Str., 52428 Jülich, Germany*
[3]*Institute of Complex Systems (ICS-5, Molecular Biophysics), Forschungszentrum Jülich, Wilhelm-Jonen-Str., 52428 Jülich, Germany*
[4]*University of Chinese Academy of Sciences, 100049 Beijing, China*
[*]*rmhuang@simm.ac.cn*

Abstract: Super-resolution imaging based on single molecule localization of cellular structures on nanometer scale requires to record a series of wide-field or TIRF images resulting in a considerable recording time (typically of minutes). Therefore, sample drift becomes a critical problem and will lower the imaging precision. Herein we utilized morphological features of the specimen (mammalian cells) itself as reference markers replacing the traditionally used markers (e.g., artificial fiduciary markers, fluorescent beads, or metal nanoparticles) for sample drift compensation. We achieved sub-nanometer localization precision <1.0 nm in lateral direction and <6.0 nm in axial direction, which is well comparable with the precision achieved with the established methods using artificial position markers added to the specimen. Our method does not require complex hardware setup, extra labelling or markers, and has the additional advantage of the absence of photobleaching, which caused precision decrease during the course of super-resolution measurement. The achieved improvement of quality and resolution in reconstructed super-resolution images by application of our drift-correction method is demonstrated by single molecule localization-based super-resolution imaging of F-actin in fixed A549 cells.

1. Introduction

Single molecule localization microscopy (SMLM), such as stochastic optical reconstruction microscopy (STORM) and its simpler variant directSTORM [1–2], and (fluorescence) photoactivation localization microscopy (PALM) [3], is based on single molecule localization and utilizes sequential activation and time-resolved localization of chemically or photoswitchable fluorophores to create super-resolution images. These techniques have opened a new era to visualize biological structures with sub-diffraction limited resolution [4–8]. To generate one SMLM image, however, one needs to record a large number of image frames and take considerable recording time (1-30 minutes). In this process, sample drift can easily be in the range of several hundreds of nanometers, which is unacceptable for super-resolution imaging, where drift is required as low as 1 nm. The reduced resolution even distorts the fine details of the reconstructed super-resolution image.

Corrections for sample drift in single molecule imaging are possible using different methods. The most widely used approach is based on imaging reference markers, typically fluorescent beads [1], metal nanoparticles [9] or fiduciary markers [10]. The stage drift is then calculated by measuring the drift of these reference markers, and can achieve localization accuracy of ≤1 nm in lateral direction and 1-10 nm in axial direction [10]. Use of these additional markers, however, can affect the single molecule localization precision due to background fluorescence,

#404123 https://doi.org/10.1364/OE.404123
Journal © 2020 Received 31 Jul 2020; revised 28 Sep 2020; accepted 4 Oct 2020; published 15 Oct 2020

Optics EXPRESS

which is also inhomogeneously distributed in the sample. Furthermore, achieving the proper concentration of beads or nanoparticles in the field of view (not too few, not too many) is difficult and unpredictable, while pattern fabrication on coverslip is complex and requires extra expense. In addition, patterns can also be concealed by sample structures. The second strategy is to use commercial systems, which are widely used in light microscopes, tracking the focus by monitoring the reflection of infrared light at the coverslip surface. This method works only properly for axial drift compensation, where the achieved axial position precision is typically not better than 20 nm. The third strategy uses a cross-correlation method to calculate the drift between the fluorescence images or reconstructed super-resolution images and can achieve 5 nm precision [11]. However, the premise of the method is that localization precision or the number of localized emitters stay constant, i.e., no permanent photobleaching of reversibly photoswitching fluorophores or no depletion of the number of irreversible photoswitching fluorophores during measurement. Since photobleaching and depletion are unavoidable, the precision of drift correction according to the third strategy is significantly reduced (especially for longer measurement time).

Here, we introduce a strategy which utilizes the diffraction information of naturally abundant circular structures inside the fixed cells in bright-field imaging mode as a reference to compensate for the three-dimensional drift. Such cellular nanostructures are for instance endosomal vesicles, lysosomes or lipid droplets, and have suitable size (couple of hundreds of nanometer). We describe how to extract the xyz position information from the nanostructures and have achieved unprecedented single-shot three-dimensional (3D) localization precision <1.0 nm in lateral direction and <6.0 nm in axial direction. We then use the 3D super-localization of nanostructures to stabilize the microscopy during directSTORM imaging. We demonstrate that the full 3D drift correction method is an alternative to the current drift compensation techniques, improving the directSTORM spatial resolution for single molecule fluorescence detection. An additional advantage of our approach manifests in the fact that it is conveniently implemented using only a simple and inexpensive commercial IR-CCD device on a second output port of the microscope. As the 3D drift correction is based on bright-field images and does not rely on fluorescence, there is no photobleaching in the correction process, thus the possible tracking time is unlimited.

2. Results

2.1. *Bright-field image patterns of circular cellular nanostructures upon change of focus*

Our stabilization method relies on monitoring the position of circular intracellular nanostructures (e.g., intracellular vesicles) in fixed A549 cells via an additional IR-CCD on the left upper port of the microscopy (Fig. 1(A)). The setup consists of a conventional inverted microscopy (Olympus IX81) and two imaging paths: IR-CCD imaging path and fluorescence imaging path. In IR-CCD imaging path, the infrared part of the output of a mercury lamp illuminates the specimen and the transmitted light is reflected by a dichroic mirror towards the left upper port of the microscopy, and then registered by the IR-CCD. In the fluorescence path, a 642 nm laser is utilized as the excitation light and the fluorescence light emitted from the specimen is separated by a dichroic mirror from the excitation light, reflected by a dielectric mirror, guided to the left lower port of the microscopy, and then collected by an EMCCD. Notably, a simple addition to regular sample preparation is incubating with poly-l-lysine for 30 minutes after fixation to further ensure vesicle stability.

The axial position of intracellular vesicles falls into one of three cases: above the focal plane, below the focal plane and in the focal plane (Fig. 1(B)). In the first case (for instance, + 600 nm), the vesicle appears as a circle darker in the center than the surrounding with a brighter external ring. In the second situation, when the z-position of the vesicle is below the focal plane (for instance, -600 nm), the vesicle image appears as a round facula brighter than the external

Optics EXPRESS

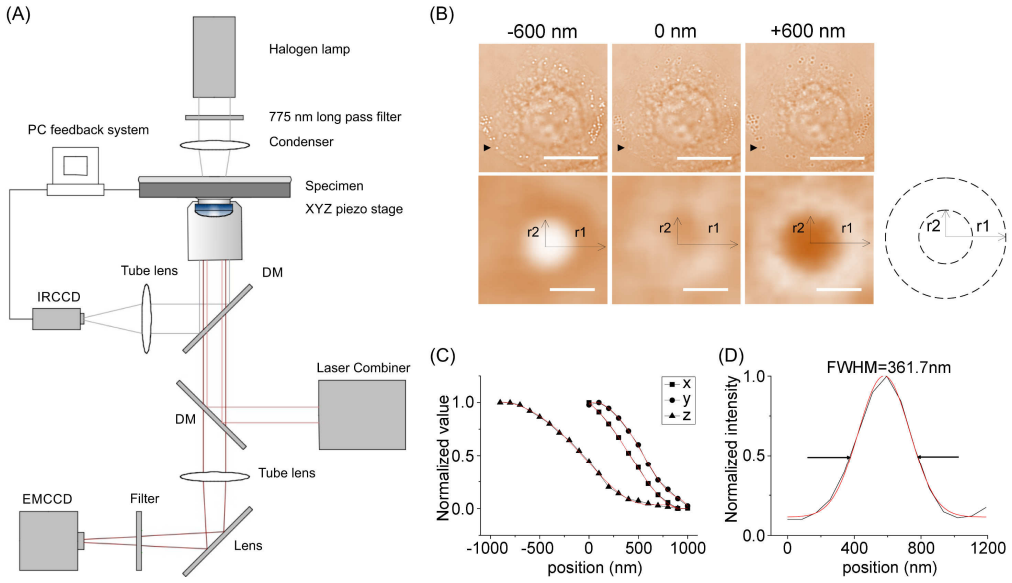

Fig. 1. Experimental setup and quantitative imaging to localize circular intracellular nanostructures. (A) Schematic of experimental setup. (B) Bright-field images of cellular structures in A549 cells when the axial positions of the specimen are set at -600 nm, 0 nm and +600 nm from the focal plane, respectively. Scale bars: 10 μm in upper images, and 500 nm in lower images. The black arrowheads in the upper panel indicate the vesicles shown in the lower panel. Radii r1 and r2 in two circular apertures around the center of the image are indicated. (C) Calibrated curves as a function of the xyz positions of a vesicle. The piezo stage is moved from 0 nm to 1000 nm in x and y directions, individually. The central positions in x and y directions are determined by the centroid algorithm and normalized. The piezo stage is moved from -1000 nm to 1000 nm in z direction. The photometric $\text{ratio}_{\text{photon}}$ in z direction is determined by the algorithm described in the main text above and then normalized. The red lines represent a fit with a six-order polynomial function to the three xyz calibration curves. (D) Size estimation of an endogenous vesicle. The line profile of the image of vesicles (black line) is achieved from the central line of the brightest facula of the vesicle in z direction (not shown in the figure), the red line represents a fit with a Gaussian function to the line profile.

background. In the third case, when the vesicle is in focus (for instance, 0 nm), the intensity of vesicle image has a nearly homogeneous distribution.

The lateral positions of vesicles (x, y) can be calculated by the centroid algorithm: $x = \sum_{ij} iI_{ij}/\sum_{ij} I_{ij}$, $y = \sum_{ij} jI_{ij}/\sum_{ij} I_{ij}$, where I_{ij} represents the intensity value in the two-dimensional pixel position (i, j) of images (Fig. 1(C)). The axial position of vesicles can be extracted from their two-dimensional diffraction images. Using two circular apertures around the center of the image with radii r1 and r2, respectively, where r1 > r2, we are able to determine the intensities in these areas and the photometric $\text{ratio}_{\text{photon}} = (I(r1) - I(r2))/I(r2)$, where I(r) represents the sum of intensity in the radii r (Fig. 1(B)). For every spot, the radii r1 and r2 are determined by $r1 = 1.86 \times \text{FWHM}$ and $r2 = 5/13 \times r1$, where FWHM (Full Width at Half Maximum) is the width of a measured curve between those points on the lateral axis which are half the maximum intensity [12,13]. The FWHM is determined from the line profile of the vesicle in x-direction (Fig. 1(D)) achieved from the central image in Fig. 1(B) where the vesicle is in focus. When the specimen is moved along the z axis, "$\text{ratio}_{\text{photon}}$" then becomes a function of the z position of the vesicle. The "$\text{z-ratio}_{\text{photon}}$" curve is shown to be nearly linear (Fig. 1(C)). Thus by the

Optics EXPRESS

calculation of $ratio_{photon}$ value from original image and comparison with the "z-$ratio_{photon}$" curve, the z position of the vesicle can be obtained in the real imaging process.

2.2. Localization precision and accuracy with endogenous vesicle

To quantify localization precision and accuracy of the method, one intracellular vesicle (361.7 nm diameter, estimated in Fig. 1(D)) inside the A549 cell is imaged and analyzed over a number of defined lateral and axial positions (Fig. 2(A)). The microscope stage is moved in steps of 100 nm at 50 Hz video rate (20 ms acquisition plus processing time per measurement) in lateral and axial directions. Two-dimensional centroid calculation algorithm and the z depth algorithm are utilized to determine the lateral and axial positions, respectively.

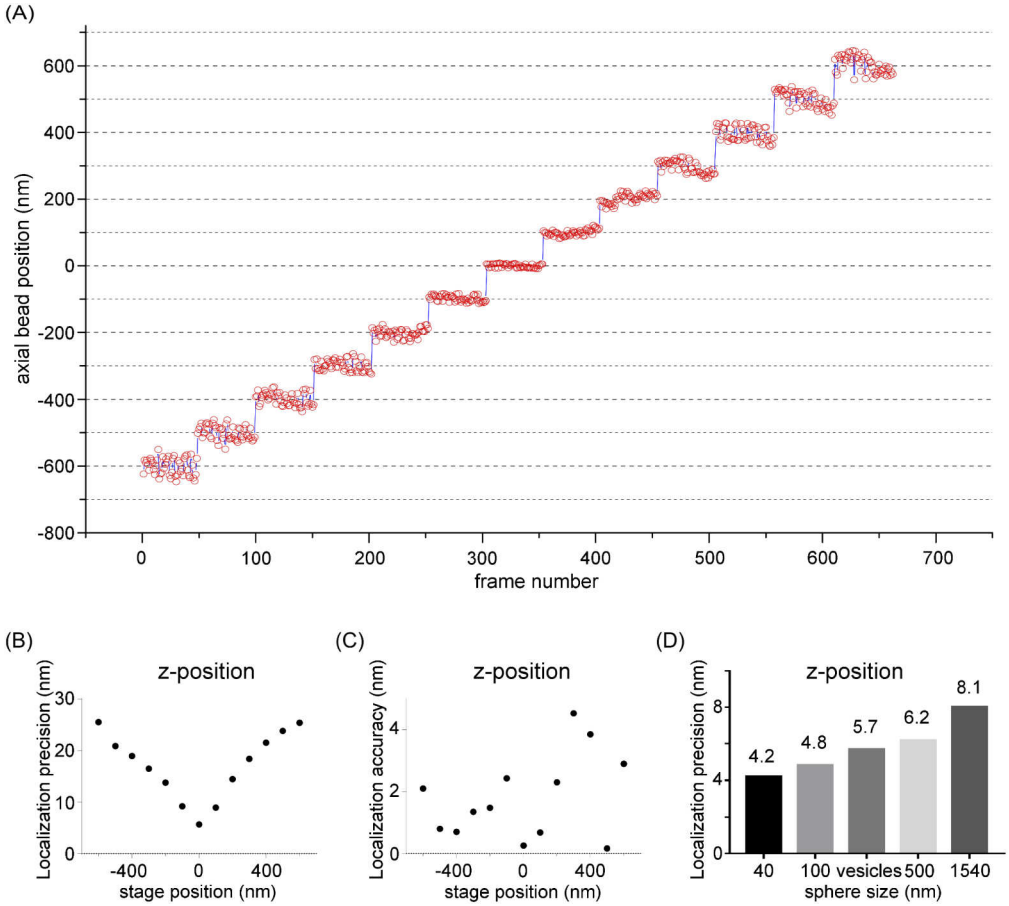

Fig. 2. The localization precision, accuracy of intracellular vesicles and external nanoparticles in z direction. (A) Comparison of measured axial positions of an endogenous vesicle (red hollow circles) at different axial displacement of the piezoelectric nano-positioning stage (black dotted line) and the average values of the experimentally determined z-positions (blue line). (B-C) Localization precision (B) and accuracy (C) of the endogenous vesicle (361.7 nm diameter) in Fig. 1(B) in z direction as a function of stage positions. (D) Comparison of localization precisions of the endogenous vesicle and four external nanoparticles with different sizes of 40 nm, 100 nm, 500 nm, and 1.54 μm in z direction.

Figure 2(A) shows the measurements of the axial positions of the vesicle compared with the displacement of the piezoelectric nano-positioning stage. A satisfactory agreement between

Optics EXPRESS

the stage position and the experimentally detected bead localization is apparent in a z-range from -600 nm to 600 nm. The localization precisions are determined as standard deviation from 50 images taken at each position. The localization precisions in x and y direction are found to be between 0.4 and 0.8 nm with no significant trend (Appendix A; Fig. 6(A), 6(D)), while the localization precision in z direction is larger (between 5 and 26 nm) and with a systematic trend (Fig. 2(B)). The localization accuracies are determined as the difference between the average calculated positions of vesicle and the real displacement of piezoelectric nano-positioning stage. The localization accuracies in x and y directions are determined to be between 0.1 and 0.6 nm (Appendix A; Fig. 6(B), 6(E)), while the localization accuracy in z direction (Fig. 2(C)) is larger (between 0 and 5 nm). No systematic trends are shown in the localization accuracy in x, y, and z directions.

2.3. Comparison with external nanoparticles

With our drift-correction method the positions of vesicles could be determined on the nano-scale. The principle is similar to the utilization of additional reference markers, such as artificial fiduciary markers, fluorescent beads, or metal nanoparticles; the difference is that the vesicles from the cell itself are utilized as the reference, and the externally added reference is not necessary. Thus it is reasonable to compare the two methods. Four external nanoparticles, including 40 nm-, 100 nm- gold nanoparticles, and 500 nm-, 1.54 μm- polymer beads, are imaged and characterized using the same method as above. Calibrated curves as functions of x, y, z position are measured, the localization precisions are determined respectively (Appendix A; Fig. 6(C), 6(F), and Fig. 2(D)) and compared with those in the endogenous vesicle (361.7 nm diameter, Fig. 1(D)). It is shown that the best localization precision of endogenous vesicle is <1.0 nm in lateral direction and <6.0 nm in axial direction. In addition, the localization precisions of these nanoparticles and endogenous vesicle show a positive association with their sizes in both lateral and axial directions, which indicates the predictable behavior that vesicles have approximately the same localization precision and accuracy as comparably sized commercial beads.

Until now, we performed the measurement from the position of only one endogenous vesicle to test the feasibility of the method. For stage drift correction, it is necessary to know the performance of multiple vesicles in the same region of interest (ROI). Therefore, we recorded the traces of three vesicles for a 200-second period (Appendix B; Fig. 7). The almost identical drift correction traces of the three vesicles (Appendix B; Fig. 7, and Appendix C; Table 1) indicate that the drift of the vesicles may be mainly depend on the drift of the microscope nano-positioning stage, but not on the intracellular vesicles themselves, which suggests that intracellular vesicles – present in all mammalian cells – are well-suited to be used as position markers in fixed cells for three-dimensional drift correction with sub-nanometer (lateral) and a-few-nanometer precision (axial), respectively, as needed for SMLM and other super-resolution fluorescence microscopy types.

We further calculated and compared the calibrated curves of five vesicles with different sizes (ranging from 335.8 nm to 412.34 nm) (Appendix D; Fig. 8). The x- and z-direction calibration curves of these intracellular vesicles are almost identical (Fig. 8(D), 8(E)), and no significant correlation between the localization precision and the vesicle size in x (Fig. 8(B)) and z direction (Fig. 8(C)) is observed (Appendix C; Table 1). Usually, the size of the different vesicle types of the endolysosomal system ranges from 20 to 2000 nm, the vast majority, however, is 50 to 500 nm large. Due to the diffraction limit and near-infrared light used for the bright-field imaging applied for drift correction, the lower limit for vesicle size in the image is between 270 and 300 nm. Therefore, the intracellular vesicles used for our drift correction method have a diameter from ~300 to 500 nm [14]. Lipid droplets, another circular intracellular nanostructure of mammalian cells are also below 1000 nm in non-adipocyte cells [15], but again the larger structures are much less abundant. Although a correlation between the localization precision and the vesicle

Optics EXPRESS

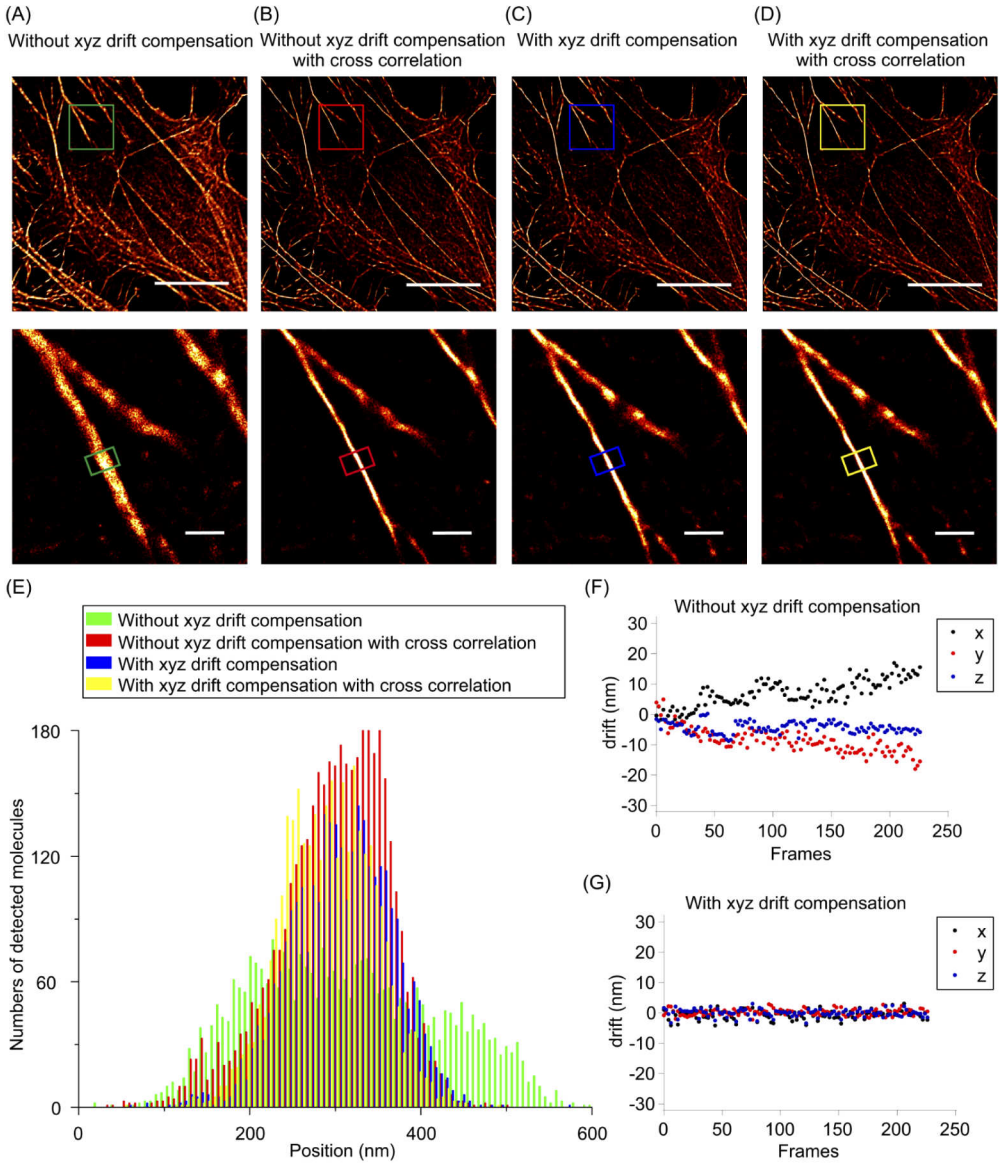

Fig. 3. Comparison of the image quality and drifts in directSTORM images between our xyz drift compensation method and the cross correlation method. (A-D) The directSTORM images for F-actin with phalloidin-Alexa Fluor 647 labelling: without xyz drift correction (A), without xyz drift correction with cross correlation algorithm (B), with xyz drift compensation (C) and with xyz drift compensation and cross correlation algorithm (D). Scale bar: 10 μm in upper panels and 1 μm in lower panels. (E) Single molecule position histograms, projected onto the long axis in boxed areas of lower panels in (A-D). (F)-(G) Drift measurements in xyz directions during the imaging of the actin filaments in A549 cell without compensation in panel (A) and with our xyz drift compensation in panel (C). The frames for drift measurement in both cases are 226 and the measurement time is around 19.4 s (86 ms/frame).

Optics EXPRESS

size is absent, an intracellular vesicle <500 nm is preferred for drift correction with our method, considering the physiological features of endogenous vesicles.

2.4. Improvement of directSTORM super-resolution images by drift correction

Next, we performed directSTORM imaging of F-actin in fixed A549 cells labelled by Alexa Fluor 647-conjugated phalloidin (Figs. 3(A)–3(D)). The super-resolution images under four conditions were compared: without xyz drift compensation (Fig. 3(A)), without xyz drift compensation with cross-correlation (Fig. 3(B)), with xyz drift compensation (Fig. 3(C)), and with xyz drift compensation with cross correlation (Fig. 3(D)). In a typical 226 frames from the whole imaging process, without xyz drift compensation the drifts of the specimen in x and y direction are beyond 20 nm and the drift in z direction is beyond 10 nm, while with xyz compensation method, the drift is suppressed to below 5 nm (Figs. 3(F), 3(G)). We choose the FWHM of actin filament as a reference to determine the image resolution, using the single molecule position histogram projecting onto the long axis. As Fig. 3(E) shown, the FWHM of a representative filament (boxed in lower panels) is determined as 316.3 nm, 137.4 nm, 142.2 nm, and 132.6 nm, under above four conditions, respectively. When there is no stabilization strategy, due to the specimen drift the distribution of the number of the detected fluorescent molecules in lateral direction is a little broad and the spatial resolution is deteriorated (Fig. 3(A)). We then apply xyz drift compensation method, without or with cross correlation algorithm for the reconstructed images (Figs. 3(C), 3(D)) [11,16]. Our xyz drift compensation alone gives a resolution that is comparable to the cross correlation algorithm without drift correction. When applying both methods together, we obtain a superior resolution with the smallest FWHM value (Fig. 3(D)). It should be noticed that the performance of the cross correlation algorithm is highly dependent on the number of emitters per frame; thus, the image resolution become worse in case of the samples with less structural details and emitters. On the contrary, our xyz drift compensation just needs the presence of a suitable intracellular vesicle.

We also concerned with the temporal dynamics related to accurate compensation for quick drift. We utilized a set of sequential directSTORM images for F-actin with an artificial drift in

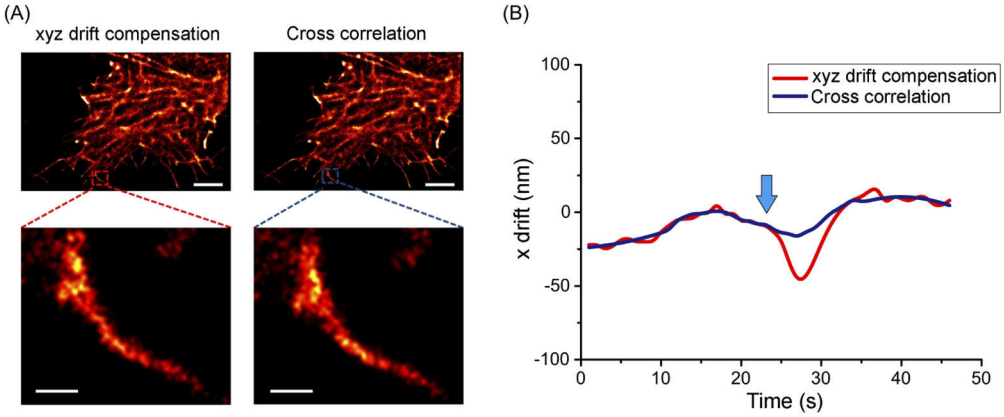

Fig. 4. Comparison of dynamic lateral accuracy between our xyz drift compensation method and the cross correlation method. (A) The reconstructed directSTORM images of F-actin in fixed A549 cells with a posteriori drift, corrected by our xyz drift compensation method and then by the cross correlation method, respectively. Scale bar: 2 μm in upper panels and 200 nm in lower panels. (B) Temporal dynamics curves of the drifts in x direction measured by our technique and by the cross correlation method. Arrow (in blue): indicating the beginning time of an artificial drift.

Optics EXPRESS

x direction, to compare our xyz drift compensation with the cross correlation method (Fig. 4). During the imaging process, a sudden and large drift (40 nm in x direction, at 23 s, driven by the piezo stage) was generated. The drifts in x direction over the whole imaging process, measured by our method or analyzed via the cross correlation method, were plotted, respectively (Fig. 4(B)). This temporal dynamics curves of the lateral drifts show the cross correlation algorithm could slightly respond to the artificial drift, while our method responds this drift and makes a complete correction (within 10 s). Notably, some fine filamentous features are better depicted in the reconstructed directSTORM image with our method than that with the cross correlation method (Fig. 4(A)). In summary, these results indicate that our method improves temporal dynamics over the cross correlation method in case of large drift occurrence.

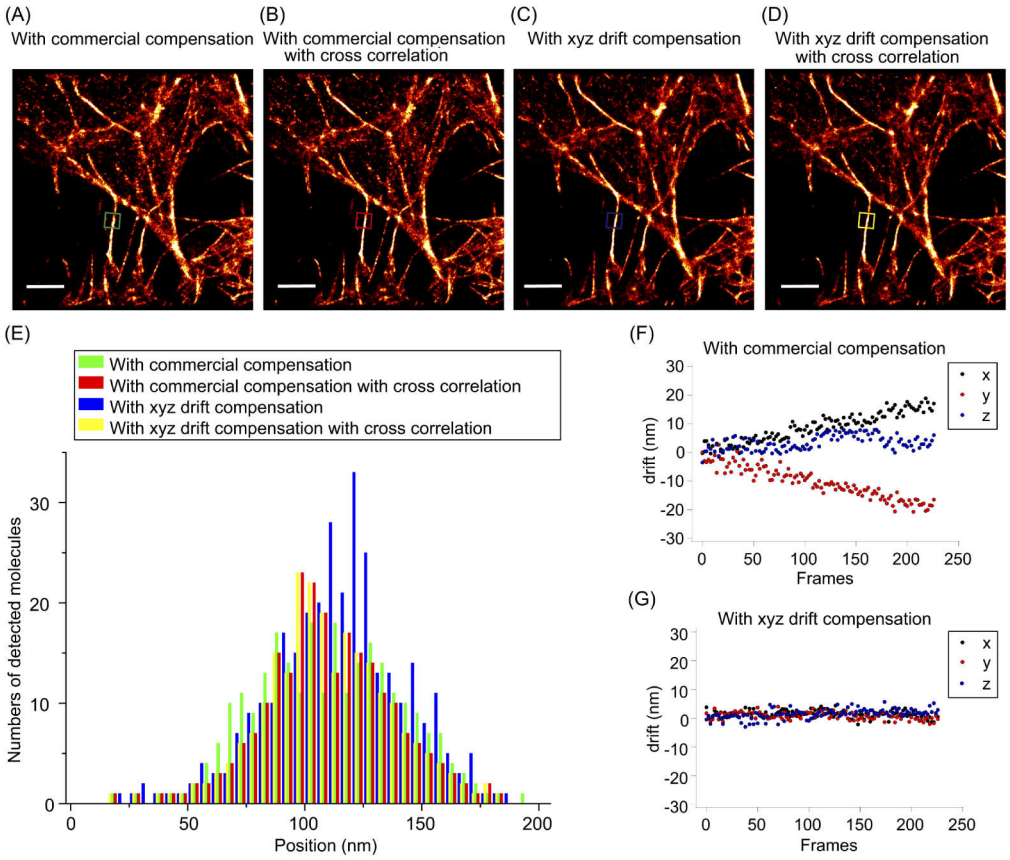

Fig. 5. Comparison of the image quality and drifts in directSTORM images between our xyz drift compensation and a commercial autofocus system. (A-D) The direct-STORM images for F-actin with phalloidin-Alexa Fluor 647 labelling: with commercial compensation (A), with commercial compensation with cross correlation (B), with xyz drift compensation (C) and with xyz drift compensation with cross correlation (D). Scale bar: 1 μm. (E) Single molecule position histograms, projected onto the long axis in boxed areas in (A-D). (F)-(G) Drift measurements in xyz directions during the imaging of the actin filaments of the A549 cell with commercial compensation in panel (A) and with xyz drift compensation in panel (C). The frames for drift measurement in both cases are 226 and the measurement time is around 19.4 s (86 ms/frame).

Optics EXPRESS

2.5. Comparison with the conventional stabilization approach

We further compared our xyz drift compensation method with a conventional approach by a commercial axial autofocus system (Nikon Perfect Focus System, Nikon, Japan). We performed directSTORM imaging of F-actin in fixed A549 cells labelled by Alexa Fluor 647 phalloidin. The reconstructed directSTORM images were acquired under four conditions: commercial compensation (Fig. 5(A)), commercial compensation with cross correlation (Fig. 5(B)), xyz drift compensation (Fig. 5(C)), and xyz drift compensation with cross correlation (Fig. 5(D)). The image obtained by commercial compensation alone shows the worst quality. Using the same quantitative method in Fig. 3(E), the FWHM of a representative tiny actin filament (boxed), whose size is beyond the diffraction limit, is determined as 85.5 nm, 68.3 nm, 56.8 nm, and 56.5 nm, respectively (Fig. 5(E)). In a typical 226 frames from the whole imaging process, with commercial compensation the drifts in x and y directions are above 20 nm and the drift in z directions is above 10 nm, whereas with our xyz drift compensation method, the drifts are reduced to below 5 nm (Figs. 5(F), 5(G)). This indicates a significant improvement of the directSTORM spatial resolution with our method, comparing with the commercial autofocus system.

3. Discussion

In summary, we have presented the principle and the application of intracellular vesicles to compensate the three-dimensional drift in super-resolution imaging. We demonstrate that the positions of vesicles can be determined with a localization precision <1.0 nm in x- and y-direction and <6.0 nm in z-direction by the usage of an IRCCD in the left port of a super-resolution fluorescence microscope detecting the bright-field image of an intracellular endogenous vesicle. The method has also been utilized for the super-resolution imaging of actin filaments, showing that the image quality, i.e., the spatial resolution of reconstructed super-resolution images has been enhanced remarkably.

The size of the usable intracellular vesicles is comparable with that of gold and polymer nanoparticles, thus we perform a comparison among them as references for our xyz drift compensation in super resolution imaging. The localization precision with intracellular vesicles is very similar to that achieved with added nanoparticles of comparable size. Therefore, the cellular component itself can be utilized as an alternative reference for xyz drift compensation. Since the reference vesicles derive from the cell itself, some difficulties existing in established methods, such as how to place proper number of reference in the field view and how to simultaneously keep the observed specimen and the reference in focus, could be solved.

Beside the easy sample preparation using our xyz drift compensation method, the additional microscope setup is also simple by using a commercial IR-CCD device only on the left output port of the microscope. There are neither complex nor expensive elements to be added and the approach is applicable to almost any microscopy without major modifications. Furthermore, as the process does not rely on fluorescence, no photobleaching occurs, which makes the tracking duration unlimited theoretically.

Herein, our xyz drift compensation method using the circular endogenous vesicles as references has been demonstrated in the fixed tumor cells for super-resolution imaging. For other mammalian cells including neurons, as well as plant cells, the method will work just as well as long as the cells are fixed. The same also holds true for many fixed bacteria and other single cell organisms, because the inclusion bodies in bacteria can be used in a similar way as the intracellular vesicles in mammalian cells. However, we estimate it may not work (or only work for very short acquisition time) in living cells, considering the movements of intracellular circular structures. Whether our method is suitable for tissue slices is highly dependent on the thickness and quality of the specimens.

Optics EXPRESS

Appendix A:

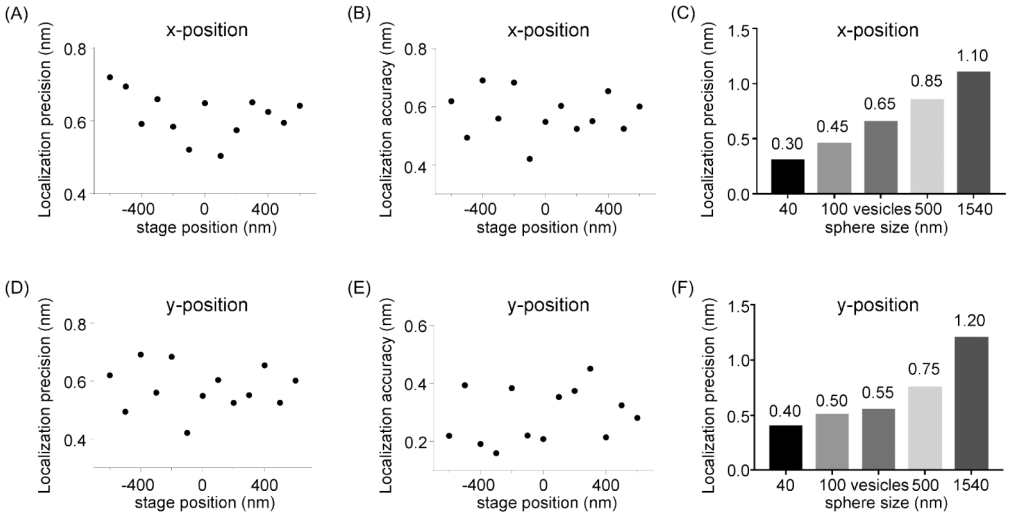

Fig. 6. The localization precision, accuracy of intracellular vesicles and external nanoparticles in x and y directions. Localization precision (A) (D) and accuracy (B) (E) of the endogenous vesicle (361.7 nm diameter) in Fig. 1(B) in x and y directions as a function of stage positions. (C) (F) Comparison of localization precisions of the endogenous vesicle and four external nanoparticles with different sizes of 40 nm, 100 nm, 500 nm, and 1.54 μm in x and y directions.

Appendix B:

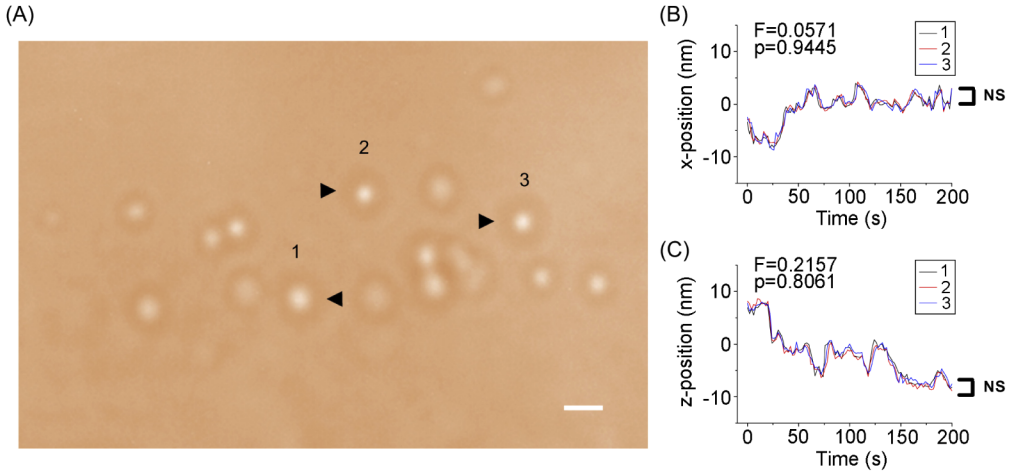

Fig. 7. Drift measured as a function of time on 3 different vesicles. (A) Three vesicles (numbered as 1, 2, and 3) on the image. Scale bar: 1 μm. (B)-(C) Drifts along the x direction (B) and z direction (C). One-way ANOVA analysis is made on the positions of these three intracellular vesicles in 200 s in x and z directions (NS: p>=0.05; also see Table 1 in Appendix C).

Optics EXPRESS

Appendix C:

Table 1. Statistical analysis for Fig. 7 and Fig. 8.

Statistical analysis	Figures	Details
One-way ANOVA	Fig. 7(B)(C)	x-position in Fig. 7(B): F=0.0571, p=0.9445; z-position in Fig. 7(C): F=0.2157, p=0.8061.
	Fig. 8(D)(E)	x-position in Fig. 8(D): F=0.009, p=0.9998; z-position in Fig. 8(E): F=0.0831, p=0.947.
Pearson correlation	Fig. 8(B)(C)	x-position in Fig. 8(B): r=0.5558, p=0.3307; z-position in Fig. 8(C): r=-0.8317, p=0.0807.

Appendix D:

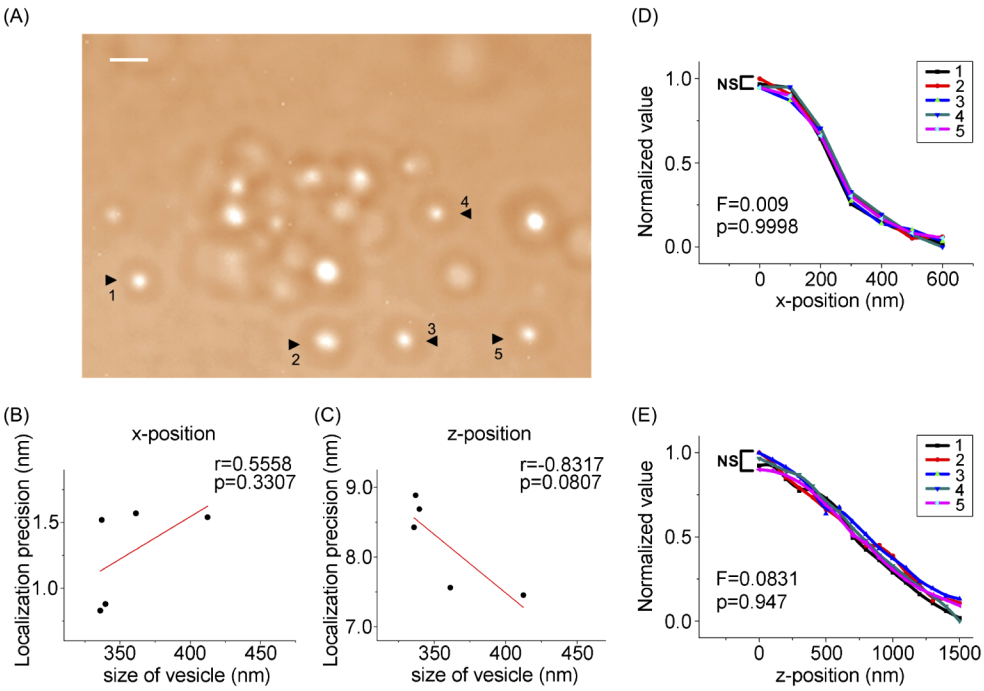

Fig. 8. Localization precision of vesicles with different sizes on the same plane. (A) The sizes of vesicles (numbered as 1-5) are 339.52 nm, 412.34 nm, 336.93 nm, 335.8 nm, and 361.24 nm, respectively. Scale bar: 1 μm. (B)-(C) Localization precision in x direction (B) and z direction (C). Pearson correlation analysis are performed and shown there are no significant correlation between the vesicle size and the localization precision (See red line in (B) and (C), also see Appendix C; Table 1. (D)-(E) Calibrated curve as a function of the x direction (D) and z direction (E) of a piezoelectric nanopositioning stage for the vesicles with No. 1-5 in (A). One-way ANOVA analysis is made on the calibrated curves of these five intracellular vesicles in x and z directions (NS: p>=0.05; also see Appendix C; Table 1).

Optics EXPRESS

Appendix E: Materials and Methods

Microscope setup. The microscope setup is based on an Olympus IX-81 inverted microscope body (Tokyo, Japan). A schematic drawing of the microscope setup is shown in Fig. 1. The samples are mounted on a nano-positioning system (p733.3DD, Physik Instrumente (PI) GmbH & Co, Karlsruhe, Germany) for axial scanning. For IR-CCD (G-223B NIR, Allied Vision, Stadtroda, Germany) imaging path, the bright field light from mercury lamp is guided to the condenser, through a filter (FGL695, Thorlabs, Dachau, Germany) and focused on the sample. The transmitted light is then reflected by a short pass edge filter (BSP01-785R-25, Semrock, Rochester, USA) and guided to the left upper port of the microscope. Then the light is focused via a tube lens (AC254-150-B, Thorlabs) and finally imaged on the IR-CCD. For fluorescence imaging, a 642 nm diode laser (MRL-III-642 nm, CNI, Changchun, China) is utilized for excitation of Alexa Fluor 647. The light is coupled into an optical fiber and is inserted into Olympus TIRF illuminator, where the TIRF angle and focus position are adjusted to proper positions so that the light is guided to the back focal plane of the microscope. The illuminated field aperture is then projected into the microscope specimen by a 100×/1.49 TIRF objective (UAPON 100× 1.49NA, Olympus) resulting in a circular illumination field of around 130 µm diameter in wide-field mode. The excitation light is reflected into the specimen by a multiband dichroic mirror set (LF635-C-000, Semrock). The emitted fluorescent light is collected through a 100× objective, a short pass edge filter (BSP01-785R- 25, Semrock), a multiband dichroic mirror (LF635-C-000, Semrock), focused via a tube lens (AC254-035-A-ML, Thorlabs), reflected via a mirror (BB1-E02, Thorlabs), filtered by a emission filter (F72-866, Analyzentechnik, Haar, Germany) and finally imaged on an EMCCD cameras (iXon, Andor Technology, Belfast, United Kingdom) which is located on the left lower port of the microscope. A program written in C language is utilized to drive the nano-positioning system in real-time for the 3D-drift correction feedback. To the axial separation between the vesicles and super resolution images, two different optical paths are used respectively: an IRCCD to record vesicle and an EMCCD to record super resolution image. At the beginning of the imaging process, the objective stage is adjusted to keep the sample in focus; then the tube lens near IRCCD is adjusted to keep the vesicle also on its focal plane.

Cell culture. A549 cells are maintained in RPMI-1640 cell medium (11875-093, ThermoFisher Scientific, Waltham, USA) with 10% (v/v) fetal bovine serum (10091-148, ThermoFisher Scientific), 1% (v/v) streptomycin/penicillin (S100JV, Shanghai Shuangda Biotechnologies, Shanghai, China) at 37°C in a humidified incubator with 5% CO_2. For vesicle imaging, 35-mm cell culture dishes (801001, NEST Biotechnology, Wuxi, China) are pretreated with 150 µl poly-l-lysine (0.1 mg/ml) for 30 min and then rinsed 3 times with sterile filtered PBS. 2×10^4 cells are seeded into each dish and directSTORM imaging is performed 24 h later.

Immunofluorescence staining. Cells are washed 4 times (5 min each time) with PBS, then fixed with 4% paraformaldehyde (PFA) for 15 min. Cells are then permeabilized with 0.5% Triton X-100 in PBS for 10 min, washed twice with PBS, and blocked with 5% (v/v) normal goat serum for 30 min. For actin staining, cells are incubated with 100 nM Alexa Fluor 647 Phalloidin solution (A22287, Invitrogen, Eugene, USA) for 60 min; then the cells are treated with 150 µl poly-l-lysine for 30 min to further stabilize the cellular structures and then rinsed 3 times with sterile filtered PBS [17].

directSTORM imaging. For directSTORM imaging, a 642 nm diode laser is used for excitation (~20 mW at back focal plane of objective, exposure time: 50 ms, pixel size: 85 nm) on Olympus IX-81 microscope (Tokyo, Japan) and Nikon N-STORM microscope (Tokyo, Japan). Series of TIRF images are recorded in each case and subsequently reconstructed for the super-resolution images. 20 µl of an oxygen scavenging solution (1 mg glucose oxidase, 1.2 µl catalase (from bovine liver), 4 mM TCEP, 5.2 mM KCl, 2 mM Tris-HCl, pH 7.5, 0.5 ml glycerol, 0.45 ml H_2O) is added into the 35-mm cell container. Then the sterile filtered PBS (pH 7.4) is

Optics EXPRESS

added until the container is completely full. ThunderSTORM software [18] is utilized to generate directSTORM image of actin filaments and calculate the drift by cross correlation algorithm.

Comparison with the cross correlation algorithm based method. To compare our xyz drift compensation method with the cross correlation algorithm-based method, we used intracellular vesicles in fixed A549 cell as references to compensate the drifts in xyz directions in real directSTORM imaging. While the cells with F-actin labelled by phalloidin-Alexa Fluor 647 are imaged sequentially: without compensation (Fig. 3(A), total 2000 frames, 86 ms/frame), and then with our xyz drift compensation (Fig. 3(C), total 1870 frames, 86 ms/frame). The cross correlation algorithm based method is utilized to both image processing (Figs. 3(B), 3(D)). For comparison purpose, the total number of detected molecules in Figs. 3(A) and 3(C) is equal in both images (total number: 1733137). The design for quick drift experiment is: 1) a sequential directSTORM acquisition is performed always with our drift compensation system for ~50 sec; 2) at the 20-sec time point, a 40-nm drift in x direction driven by the piezo stage is generated; 3) this drift is then corrected by our compensation system within ~10 sec; 4) After acquisition finished, the physical movements in x direction of the stage for drift correction is also recorded; 5) The post-imaging cross correlation method is also applied to the set of sequential directSTORM images during the whole process.

Comparison with conventional drift correction techniques. To compare our xyz drift compensation method with conventional drift correction techniques, we use a commercial autofocus approach (Nikon Perfect Focus System, Nikon, Japan) to track only the axial defocus, and then use our method to track and compensate the xyz drifts. The same fixed A549 cell with F-actin labelled by phalloidin-Alexa Fluor 647 is imaged sequentially using the conventionally used compensation technique (Fig. 5(A), total 2000 frames, 86 ms/frame), and then our xyz drift compensation method (Fig. 5(C), total 1702 frames, 86 ms/frame). The cross correlation algorithm based method is utilized to both images processing (Figs. 5(B), 5(D)) For comparison purpose, the total number of detected molecules in Figs. 5(A) and 5(C) is equal in both images (total number: 119348).

Funding

National Natural Science Foundation of China (81771890, 91859106); The National Science & Technology Major Project "Key New Drug Creation and Manufacturing Program", China (2018ZX09711002-010-001); One Hundred Talent Program of Chinese Academy of Sciences; Instrument Function Development Project of Chinese Academy of Sciences.

Acknowledgments

We thank technical supports from the Institutional Technology Service Center of Shanghai Institute of Materia Medica, Chinese Academy of Sciences, Yang Yu, Yan Wang and Yao Li from Integrated Laser Microscopy System at National Facility for Protein Science in Shanghai, Zhangjiang Laboratory (NFPS, ZJLab), China.

Disclosures

The authors declare no conflicts of interest.

References

1. M. J. Rust, M. Bates, and X. Zhuang, "Sub-diffraction-limit imaging by stochastic optical reconstruction microscopy (STORM)," Nat. Methods **3**(10), 793–796 (2006).
2. S. van de Linde, A. Loschberger, T. Klein, M. Heidbreder, S. Wolter, M. Heilemann, and M. Sauer, "Direct stochastic optical reconstruction microscopy with standard fluorescent probes," Nat. Protoc. **6**(7), 991–1009 (2011).
3. E. Betzig, G. H. Patterson, R. Sougrat, O. W. Lindwasser, S. Olenych, J. S. Bonifacino, M. W. Davidson, J. Lippincott-Schwartz, and H. F. Hess, "Imaging intracellular fluorescent proteins at nanometer resolution," Science **313**(5793), 1642–1645 (2006).

Optics EXPRESS

4. E. Abbe, "Beiträge zur Theorie des Mikroskops und der mikroskopischen Wahrnehmung," Archiv f. mikrosk. Anatomie **9**(1), 413–468 (1873).
5. L. Rayleigh, "On the theory of optical images, with special reference to the microscopy," J. R. Microsc. Soc. **23**(4), 474–482 (1903).
6. K. Xu, G. Zhong, and X. Zhuang, "Actin, spectrin, and associated proteins form a periodic cytoskeletal structure in axons," Science **339**(6118), 452–456 (2013).
7. A. Pertsinidis, K. Mukherjee, M. Sharma, Z. P. Pang, S. R. Park, Y. Zhang, A. T. Brunger, T. C. Sudhof, and S. Chu, "Ultrahigh-resolution imaging reveals formation of neuronal SNARE/Munc18 complexes in situ," Proc. Natl. Acad. Sci. U. S. A. **110**(30), E2812–E2820 (2013).
8. T. Appelhans, C. P. Richter, V. Wilkens, S. T. Hess, J. Piehler, and K. B. Busch, "Nanoscale organization of mitochondrial microcompartments revealed by combining tracking and localization microscopy," Nano Lett. **12**(2), 610–616 (2012).
9. P. Bon, N. Bourg, S. Lecart, S. Monneret, E. Fort, J. Wenger, and S. Leveque-Fort, "Three-dimensional nanometre localization of nanoparticles to enhance super-resolution microscopy," *Nat. Commun.* 67764 (2015).
10. S. H. Lee, M. Baday, M. Tjioe, P. D. Simonson, R. B. Zhang, E. Cai, and P. R. Selvin, "Using fixed fiduciary markers for stage drift correction," Opt. Express **20**(11), 12177–12183 (2012).
11. Y. N. Wang, J. Schnitzbauer, Z. Hu, X. M. Li, Y. F. Cheng, Z. L. Huang, and B. Huang, "Localization events-based sample drift correction for localization microscopy with redundant cross-correlation algorithm," Opt. Express **22**(13), 15982–15991 (2014).
12. M. Capitanio, R. Cicchi, and F. S. Pavone, "Position control and optical manipulation for nanotechnology applications," Eur. Phys. J. B **46**(1), 1–8 (2005).
13. C. Franke, M. Sauer, and S. V. van de Linde, "Photometry unlocks 3D information from 2D localization microscopy data," Nat. Methods **14**(1), 41–44 (2017).
14. J. Klumperman and G. Raposo, "The Complex Ultrastructure of the Endolysosomal System," Cold Spring Harbor Perspect. Biol. **6**(10), a016857 (2014).
15. M. Suzuki, Y. Shinohara, Y. Ohsaki, and T. Fujimoto, "Lipid droplets: size matters," Microscopy **60**(Suppl 1), S101–S116 (2011).
16. M. Mirzaei, A. Asif, M. Fortin, and H. Rivaz, "3D normalized cross-correlation for estimation of the displacement field in ultrasound elastography," Ultrasonics **102**, 106053 (2020).
17. K. Colville, N. Tompkins, A. D. Rutenberg, and M. H. Jericho, "Effects of Poly(L-lysine) Substrates on Attached Escherichia coli Bacteria," Langmuir **26**(4), 2639–2644 (2010).
18. M. Ovesny, P. Krizek, J. Borkovec, Z. Svindrych, and G. M. Hagen, "ThunderSTORM: a comprehensive ImageJ plug-in for PALM and STORM data analysis and super-resolution imaging," Bioinformatics **30**(16), 2389–2390 (2014).